Inorganic Chemistry
Cite This: Inorg. Chem. XXXX, XXX, XXX−XXX
Article
pubs.acs.org/IC

β-Na_2TeO_4: Phase Transition from an Orthorhombic to a Monoclinic Form. Reversible CO_2 Capture

Cyrille Galven,[†] Thierry Pagnier,[‡] Noël Rosman,[‡] Françoise Le Berre,[†] and Marie-Pierre Crosnier-Lopez*,[†]

[†]Institut des Molécules et Matériaux du Mans (IMMM), UMR CNRS 6283, Le Mans Université, Avenue Olivier Messiaen, 72085 Le Mans CEDEX 9, France

[‡]Université Grenoble Alpes, Université Savoie Mont Blanc, CNRS, Grenoble INP, LEPMI, 38000 Grenoble, France

Supporting Information

ABSTRACT: The present work concerns the tellurate Na_2TeO_4 which has a 1D structure and could then present a CO_2 capture ability. It has been synthesized in a powder form via a solid-state reaction and structurally characterized by thermal X-ray diffraction experiments, Raman spectroscopy, and differential scanning calorimetry. The room temperature structure corresponds to the β-Na_2TeO_4 orthorhombic form, and we show that it undergoes a reversible structural transition near 420 °C toward a monoclinic system. Ab initio computations were also performed on the room temperature structure, the Raman vibration modes calculated, and a normal mode attribution proposed. In agreement with our expectations, this sodium oxide is able to trap CO_2 by a two-step mechanism: Na^+/H^+ exchange and carbonation of the released sodium as $NaHCO_3$. This capture is reversible since CO_2 can be released upon heating by recombination of the mother phase.

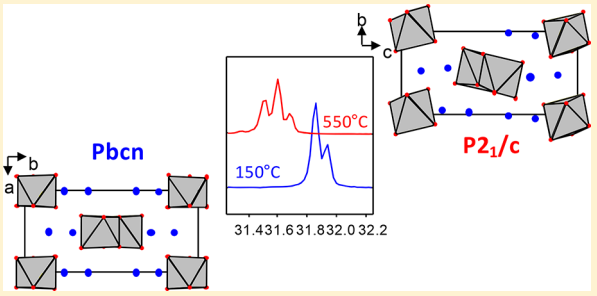

INTRODUCTION

The capture and recycling of atmospheric CO_2 is a major goal in the fight for a cleaner world.[1] Numerous technologies have been described for this purpose in the literature (absorption with a solvent, selective membrane separation, CO_2 absorbents for example). Among CO_2 absorbents, oxides containing alkali metals can be used as CO_2 traps,[2−4] trapping which can also be reversible,[5] allowing thus cyclic processes of CO_2 capture and use. If a few lithium oxides have been studied for this application in the last 10 years,[6−10] then some studies[11,12] have shown that sodium use is preferable to lithium: For example, Na_2ZrO_3 presents much better properties for CO_2 capture than those of lithium zirconate. Moreover, sodium is more abundant than lithium and therefore cheaper. Then, in the search for new materials able to capture CO_2, we focused on sodium-based oxide and in particular compounds in which the sodium ions must be able to leave the oxide structure. This will be best done with materials of low dimensionality, containing chains or planes of structure oxide groups. This is the reason why we were interested in tellurates containing Te with a +VI formal oxidation level. Indeed, these compounds, which are nowadays extensively investigated as new LTCC (low-temperature co-fired ceramics) dielectric systems for microwave applications,[13] crystallize in various dimensionality, from 0D (isolated octahedra, H_6TeO_6) to 1D (chains of TeO_6 octahedra, Na_2TeO_4), to 2D (planes of TeO_6 octahedra, H_2TeO_4) or even 3D (β-TeO_3). Reference 13 lists many of these materials.

The tellurate Na_2TeO_4 which has a 1D structure with the Na^+ ions located between $[TeO_4]_n^{2n-}$ chains can be therefore a good candidate for the CO_2 capture via a Na^+/H^+ exchange. This mechanism has been detailed in works on lithium oxides for which the CO_2 capture ability was associated with a Li^+/H^+ exchange and the formation of Li_2CO_3.[10−18] In Na_2TeO_4, the Na^+/H^+ exchange has been proved to be reversible by Kratochvil and Jensovsky:[19] They obtain their Na_2TeO_4 crystals by slow dehydration of $Na_2H_4TeO_6$ in an $NaNO_3$ melt from 300 °C, and those Na_2TeO_4 crystals spontaneously rehydrate in wet atmosphere or in water to give $Na_3H_5Te_2O_{10}$. This indicates clearly that Na^+ ions are mobile in the structure, a prerequisite for the CO_2 capture through the formation of $NaHCO_3$.

In 1977, the crystallographic structure of Na_2TeO_4 was determined concurrently by two groups with two different results. While Kratochvil and Jensovsky[19] found an orthorhombic structure (*Pbcn*; 5.798, 12.24, and 5.214 Å), Daniel et al.[20] obtained a monoclinic one ($P2_1/c$; 10.632, 5.161, and 13.837 Å, $\beta = 103.27°$) under hydrothermal conditions from a mixture of NaOH and TeO_2 at 600 °C. In 1985, Lapasset et al. confirmed the dimorphism of Na_2TeO_4[21] and concluded that the transition from one form (α-Na_2TeO_4, monoclinic) to the other (β-Na_2TeO_4, orthorhombic) was difficult and irreversible, due to a need for large rotations and translations of some of the

Received: April 12, 2018

DOI: 10.1021/acs.inorgchem.8b00993
Inorg. Chem. XXXX, XXX, XXX−XXX

TeO_6 chains, despite their probably very close energy. In 2000, another preparation way was published:[22] It corresponds to a ceramic route which consists of heating at 600 °C of a mixture of Na_2CO_3 and TeO_2. Unfortunately, no structural details were given except the cell parameters of a new orthorhombic cell (10.602, 10.622, and 8.506 Å). In addition, the authors give one table with 12 *hkl* and their corresponding d_{obs} and d_{cal}, but our refinement performed from these few data does not lead to their published parameters. More recently, a new Na_2TeO_4 form (denoted as γ-form, orthorhombic *Pnna*: 13.5390, 8.4169, and 6.7781 Å) was obtained by Weil et al.[23] as minority phase from treatment of $Ba[TeO_2(OH)_4]$ in a $NaNO_3$ melt. Nevertheless, whatever the synthesis mode (except that of the ref 22), the three Na_2TeO_4 polymorphs contain edge-sharing TeO_6 octahedra forming $[TeO_4]_n^{2n-}$ chains and could then be interesting candidates toward CO_2 capture.

In addition to the CO_2 capture property, we present in this paper the thermal stability of the β-Na_2TeO_4 orthorhombic form. Furthermore, except for a room temperature Raman spectrum appearing in Cornette's thesis,[13] there was no work on Na_2TeO_4 vibrational properties. The Raman spectrum was then measured as a function of temperature while ab initio computations were performed on the crystallographic structures that we determined in order to compare their energy.

EXPERIMENTAL SECTION

Synthesis. We chose to prepare our β-Na_2TeO_4 sample via a solid-state reaction. Powders of TeO_2 (Acros Organics, 99.8%) and dried Na_2CO_3 (Alfa Aesar, 99.99%) in stoichiometric ratio were intimately mixed in an agate mortar and pressed into pellets. The pellets (1 g; diameter: 10 mm) were placed in an alumina crucible and heated two times at 650 °C for 12 h in air. Powder X-ray diffraction (PXRD) analysis was used after each heating cycle to check the completeness of the reaction as well as the crystallinity and the purity of the product. After the synthesis, the obtained white powder was kept immediately in a dryer to prevent any unwanted hydration taking into account the study of Kratochvil and Jensovsky.[19]

Powder X-ray Diffraction. For the structural room temperature (RT) study, powder X-ray diffraction (PXRD) data were collected in air with a PANalytical X'pert Pro diffractometer using Cu Kα radiation equipped with a X'Celerator detector with the following experimental conditions: angular range, 2θ = 13.55−150.00°; step scan increment, 2θ = 0.0084°; counting time = 12 h.

For the thermal analysis, a PANalytical Empyrean diffractometer equipped with a high-temperature attachment HRK900 was used with the Cu Kα radiation. The data were collected under dry air flow every 50 °C between 50 and 600 °C with the following experimental conditions: angular range, 2θ = 13.00−148.00°; step scan increment, 2θ = 0.0131°; counting time = 6 h.

All the refinements were performed with the Rietveld method[24] using the Fullprof program,[25] and a pseudo-Voigt function was chosen to model the peak shape. The background points were determined manually before being refined.

Raman Spectroscopy. The Na_2TeO_4 Raman spectra were collected on a pellet with a Renishaw InVia Raman spectrometer in backscattering mode. The exciting source was an Ar laser operating at the 514.5 nm green light. The sample was illuminated through a ×50 objective with a long (8 mm) working distance. Raman spectra down to about 7 cm^{-1} were obtained with the use of superNotch filters. The detector was a Peltier-cooled CCD. For the temperature measurements, a Linkam THMS600 cell was used. In order to accurately measure the sample temperature, we placed a small silicon piece close to the sample. The temperature was then calculated according to the Si 520 cm^{-1} band position as described in ref 26.

Thermal Analysis. Differential scanning calorimetry (DSC, 92 Setaram) was used in order to precisely determine the thermal behavior of Na_2TeO_4. For this study performed under N_2 flow, the sample has been heated from RT to 550 °C at a rate of 10 °C min^{-1} and cooled from 550 °C to RT at the same rate.

The TGA curve has been registered between RT and 550 °C on a TGA Jupiter STA 449 F3 Netzsch instrument coupled with a mass spectrometer Aëlos QMS 403C Netzsch allowing the analysis of gas emitted by the sample during heating.

Ab Initio Calculations. Ab initio calculations were performed with the ABINIT software.[27] A Perdew−Burke−Ernzerhof GGA functional[28] was used for the exchange-correlation calculations. FHI pseudopotentials[29] were obtained from the Abinit Web site. The energy cutoff was held at 45 Ha (1224 eV) and the k-points grid was that proposed by the software, containing 4 independent k-points. Raman vibrational frequencies and normal modes were calculated using generalized forces as described in the Supporting Information. A correcting factor of 1.077 was applied to the calculated frequencies to take into account the underestimation inherent to the technique. This factor was chosen to minimize the distance between observed and calculated Ag modes.

Scanning Electron Microscopy (SEM) Analysis. SEM images were obtained using a JSM 6510 LV microscope (JEOL) equipped with an energy-dispersive X-ray (EDX) OXFORD detector (AZtec software) to perform elementary microanalyses. For SEM observations, the particles were coated with gold.

RESULTS AND DISCUSSION

Characterization of the Room Temperature Phase. The different PXRD patterns registered have rapidly revealed that this compound presented a strong preferential orientation. This is clearly showed in Figure 1 where two PXRD patterns

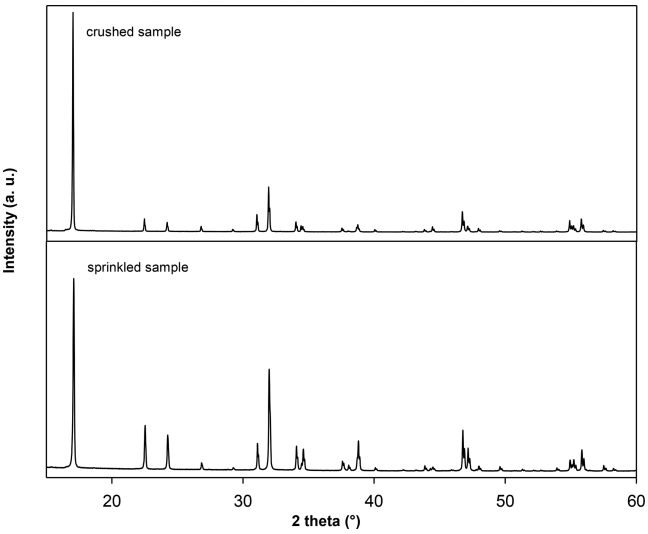

Figure 1. PXRD pattern of Na_2TeO_4 at room temperature showing the strong preferential orientation in the case of a crushed sample.

are presented: one with a crushed sample and a second one with a sprinkled sample. We indeed observe significant differences in the relative intensities of the *hkl* lines on the two diagrams. This preferential orientation can be explained by the elongated platelet aspect of the grains evidenced by SEM image (see Figure S1). This lead us to perform the structural study at room temperature with the data obtained from a carefully sprinkled sample on grease to promote a random orientation of the crystallites. The *hkl* lines are narrow, indicating a good crystallization of the powder sample. In addition, the purity of the sample is quite good since all the lines could be indexed in the orthorhombic *Pbcn* (no. 60) space group with refined cell parameters (a = 5.75845(2), b =

DOI: 10.1021/acs.inorgchem.8b00993
Inorg. Chem. XXXX, XXX, XXX−XXX

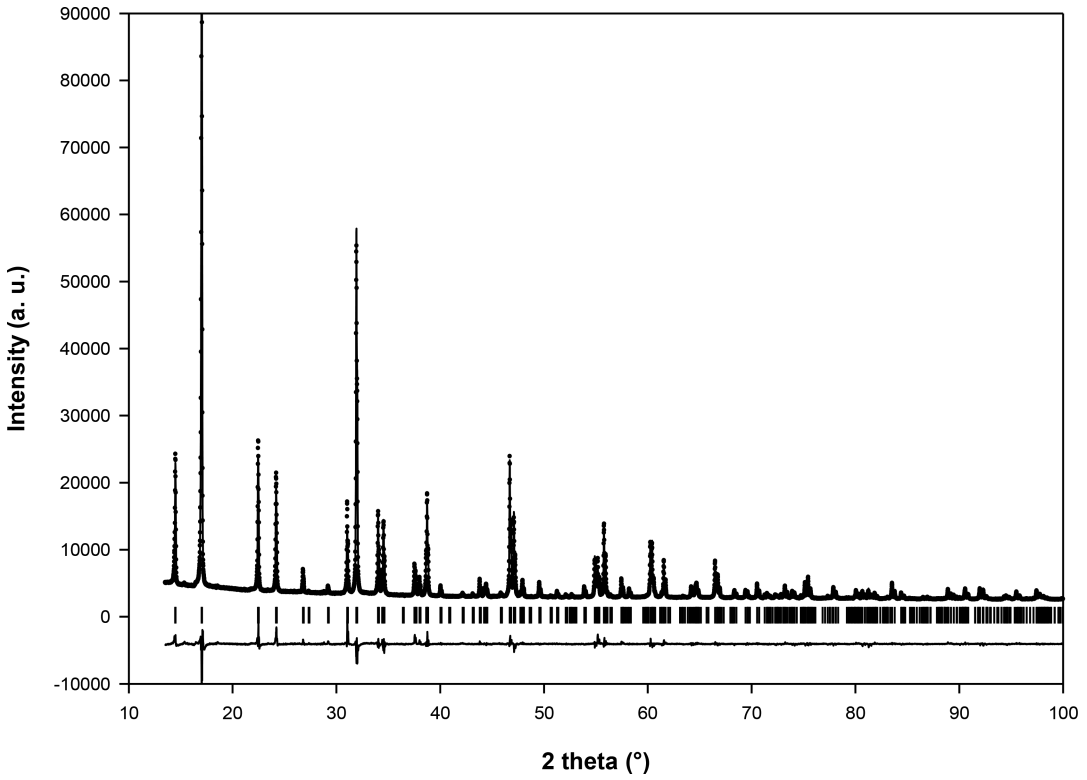

Figure 2. Observed, calculated, and difference PXRD patterns of β-Na_2TeO_4 (sprinkled sample) at room temperature in the *Pbcn* SG. Vertical bars are related to the Bragg reflections positions.

Table 1. Room Temperature Structure Data of Na_2TeO_4 Obtained by Rietveld Refinement[a]

space group *Pbcn* (no. 60)
a = 5.75845(2) Å, b = 12.22603(5) Å, c = 5.18998(2) Å
[a = 5.757 Å, b = 12.207 Å, c = 5.229 Å]
R_p = 11.1, R_{wp} = 10.9, R_{exp} = 5.19, χ^2=4.39, Bragg R-factor = 5.36
η = 0.615(6); half-width parameters: u = 0.0121(3), v = −0.0111(3), w = 0.0086(1)

atom	site	x	y	z	B_{iso}
Te	4c	0	0.07152(4) [0.0723]	1/4	1.15(1)
Na1	4c	0	0.7717(2) [0.7746]	1/4	2.62(4)
Na2	4c	0	0.3610(2) [0.3610]	1/4	2.62(4)
O1	8d	0.3012(6) [0.2982]	0.3262(3) [0.3258]	0.6150(6) [0.6117]	1.47(5)
O2	8d	0.3190(5) [0.3202]	0.5476(3) [0.5506]	0.5723(6) [0.5710]	1.47(5)

[a]The results of the ab initio calculations are given in square brackets.

12.22603(5), and c = 5.18998(2) Å) in agreement with the β-Na_2TeO_4 form of ref 19.

We decided then to start the Rietveld calculations with the Na_2TeO_4 structural model published by Kratochvil and Jensovsky.[19] With one isotropic temperature factor attributed for each kind of atom, the agreement between calculated and experimental patterns is good with the final reliability factors: R_p = 11.1, R_{wp} = 10.9, R_{exp} = 5.19, χ^2=4.39, Bragg R-factor = 5.36 (Figure 2). The structural refinement results are given in Table 1 with atomic coordinates and isotropic temperature factors, while selected interatomic distances and bond valence sums[30] are gathered in Table 2.

The crystal structure can be described as built up from infinite chains of $Te^{VI}O_6$ octahedra sharing edges parallel to the c axis (Figure 3). The chains of $[TeO_4]_n^{2n-}$ formulation are linked together by the sodium cations in a very distorted octahedral coordination. The Te−O distances range from 1.835(4) to 2.014(3) Å with a mean distance of 1.953 Å. This value is consistent with the sum of the ionic radii (1.96 Å) from Shannon's table[31] and leads to a bond valence sum equal to 5.7 instead of the formal value of 6. Classically, the two shortest Te−O distances correspond to the terminal O^{2-} ion (O1) which is not linked to the neighboring Te of the $[TeO_4]_n^{2n-}$ chain. In the distorted NaO_6 octahedra, Na−O distances range from 2.221(4) to 2.611(4) Å for Na1 and from 2.340(3) to 2.653(4) Å for Na2, leading to mean distances respectively equal to 2.381 and 2.532 Å which can be compared to the corresponding sum of the ionic radii:[31] 2.42 Å. For the two sodium sites, the calculated bond valence sums are respectively 1.4 and 0.9 for Na1 and Na2 (expected value: 1). All these values are very close to those obtained from the single crystal study: The bond valence sums of Te, Na1 and Na2 calculated from the atomic positions of ref 19 are respectively equal to 5.6, 1.4, and 0.9. We can note here that the two sodium ions are clearly not equivalent, which may have an effect on their mobility thereafter.

DOI: 10.1021/acs.inorgchem.8b00993
Inorg. Chem. XXXX, XXX, XXX−XXX

Table 2. Selected Interatomic Distances (Å) and Bond Valence Sums ($\Sigma\nu$) for Na_2TeO_4 at Room Temperature (S.G.: *Pbcn*) and at 550°C ($P2_1/c$)[a]

Te octahedra		Na octahedra	
RT	550 °C	RT	550 °C
Te−O1: 2 × 1.835(4)	Te−O2: 1.892(6)	Na1−O1: 2 × 2.221(4)	Na1−O1: 2.074(8)
Te−O2: 2 × 1.993(3)	Te−O4: 1.944(7)	Na1−O1: 2 × 2.311(3)	Na1−O2: 2.247(9)
Te−O2: 2 × 2.014(3)	Te−O3: 1.951(6)	Na1−O2: 2 × 2.611(4)	Na1−O2: 2.287(9)
⟨*Te−O*⟩ = *1.953 Å*	Te−O1: 1.983(6)	⟨*Na1−O*⟩ = *2.381 Å*	Na1−O3: 2.534(8)
$\Sigma\nu$ = 5.7, $\Sigma\nu_{expected}$ = 6	Te−O3: 2.096(6)	$\Sigma\nu$ = 1.4, $\Sigma\nu_{expected}$ = 1	Na1−O1: 2.699(8)
	Te−O4: 2.148(7)		⟨*Na1−O*⟩ = *2.37 Å*
	⟨*Te−O*⟩ = *2.00 Å*		(Na1−O4: 2.948(8))
		Na2−O2: 2 × 2.340(3)	Na2−O4: 2.259(8)
		Na2−O1: 2 × 2.603(3)	Na2−O3: 2.357(8)
		Na2−O1: 2 × 2.653(4)	Na2−O2: 2.512(7)
		⟨*Na2−O*⟩ = *2.532 Å*	Na2−O1: 2.523(8)
		$\Sigma\nu$ = 0.9, $\Sigma\nu_{expected}$ = 1	Na2−O4: 2.772(8)
			⟨*Na2−O*⟩ = *2.49 Å*
			(Na2−O2: 2.930(8))

[a]Mean distances are given in italic.

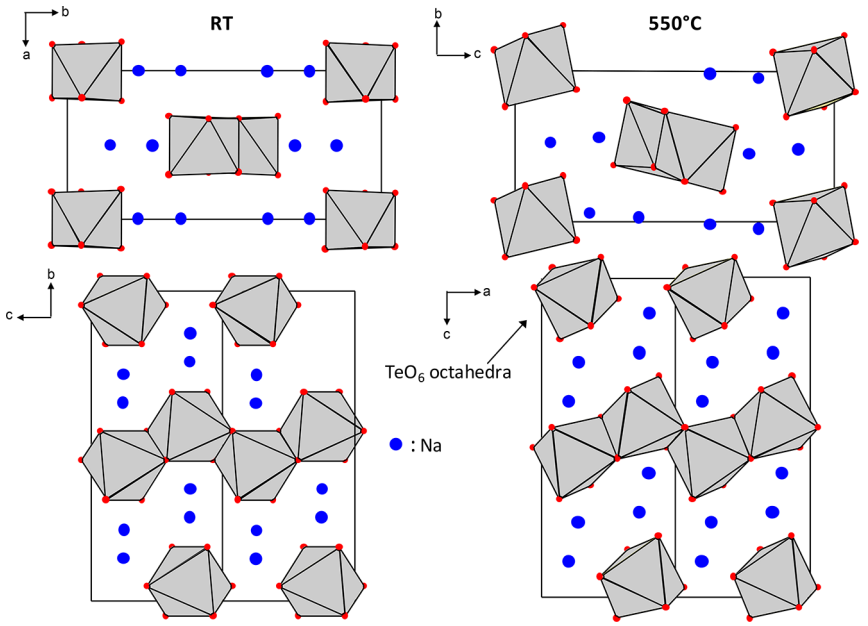

Figure 3. Projection of the Na_2TeO_4 structures showing the $[TeO_4]_n^{2n-}$ chains.

Figure 4 shows the Raman spectrum of Na_2TeO_4 at room temperature together with its decomposition into Lorentzian bands. It has to be pointed out that band intensities varied from point to point, indication of local preferential orientations of the grains. Apart of this, the experimental spectrum is identical to the one published by Cornette in her thesis.[13] From the group theory, 42 vibrations are expected to be Raman-active (9 A_g, 12 B_{1g}, 9 B_{2g}, 12 B_{3g}). Twenty-three bands have been observed on the experimental spectrum. The band wavenumbers obtained experimentally are listed in Table 3, together with the calculated values obtained by Cornette with the LADY software[13] and those obtained by our ab initio calculations. All these results agree fairly well, which confirms the orthorhombic structure of β-Na_2TeO_4 at room temperature prepared by the solid-state reaction from TeO_2 oxide and Na_2CO_3 carbonate.

The band attributions are also provided in Table 3. In many cases, two bands belonging to two different symmetries appear very close to each other, A_g with B_{2g} and B_{1g} with B_{3g}. This is particularly clear at high frequencies. The highest frequencies correspond to Te-non bridging oxygen O1 stretching. Surprisingly, the second group (647.7−673.0 cm^{-1}) corresponds to a O2−O2 stretch, suggesting a rather strong bond between these two oxygen atoms. Te−O2 stretching frequencies appear slightly below, near 520 cm^{-1}. The Na1 translations appear between 300 and 236 cm^{-1}, while those of Na2 appear at lower frequencies, below 230 cm^{-1}. For the atomic displacements ab initio calculated for all modes; see Tables S1−S4.

Structure evolution with temperature. Figure 5 shows the evolution of the PXRD patterns obtained when heating the sample up to 600 °C. A change is highlighted between 350 and 450 °C corresponding simultaneously to the appearance of a set of new *hkl* lines and a peak splitting (for example near 2θ = 31.5°) leading to a lowering of the symmetry. This trans-

DOI: 10.1021/acs.inorgchem.8b00993
Inorg. Chem. XXXX, XXX, XXX−XXX

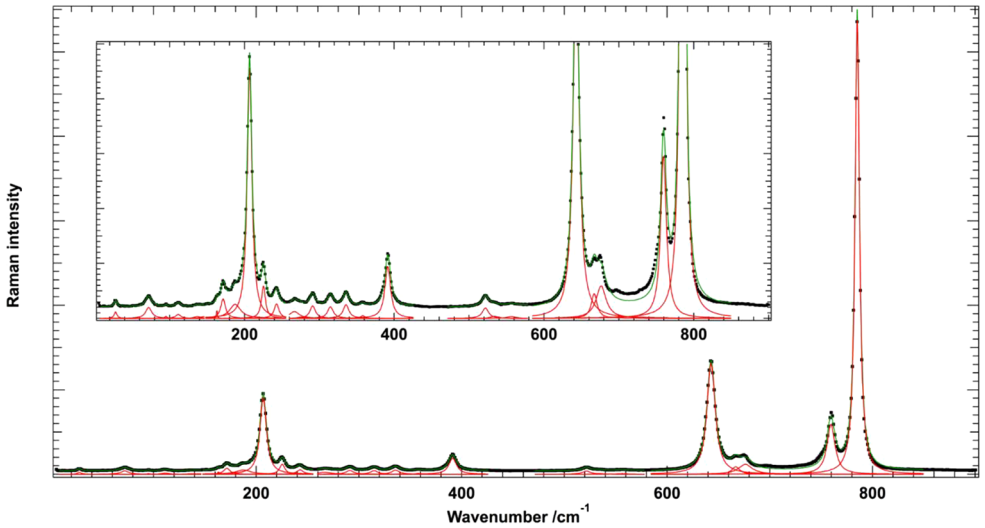

Figure 4. Raman spectrum of Na_2TeO_4 at room temperature. Insert: expanded view of the low intensity region.

formation is reversible since the PXRD pattern obtained at room temperature after this heating can be indexed in the mother cell with the initial *Pbcn* (no. 60) space group. In addition, this phase transition is also well observed by thermal analysis: While no weight loss can be depicted between RT and 650 °C on the TGA curve, the DSC graph clearly shows a reversible peak at 421 °C on heating and 420 °C on cooling (Figure 6), a peak which can be unambiguously associated to the structural transition observed on PXRD patterns.

In good agreement with those observations, while the PXRD patterns obtained between RT and 400 °C can be refined successfully in the initial orthorhombic cell using the *Pbcn* space group, the PXRD patterns registered at higher temperature (450−600 °C) require the use of a monoclinic cell to index all the observed *hkl* lines. The Figure 7 gives the evolution versus temperature for each cell parameter: If the cell parameter parallel to the chains axis (close to 5.2 Å) remains nearly constant, then the two others increase leading to a continuous evolution of the cell volume. Nevertheless, a careful examination of these four evolutions shows an accident at the transition temperature. The refined cell parameters and the cell volume for each temperature are gathered in Table S5.

Figure 8 shows the Raman spectra obtained during heating in dry synthetic air. The high-frequency modes do not vary much, except for a band widening evidenced clearly above 400 °C. At low frequency, however, changes are more drastic, with an apparent splitting of the band near 200 cm^{-1} and the appearance of a very strong band at low frequency, close to 18 cm^{-1}. All these changes are fully reversible, with no hysteresis.

Characterization of the High Temperature Structure. As it is impossible at high temperature to use grease to limit the preferential orientation, we tried in a first time to quench the sample to stabilize the high temperature form at RT. Unfortunately, even the quench in liquid nitrogen (sample placed in a sealed platinum tube) did not allowed to retain the monoclinic structure. The structural study has then been performed with a diffractometer equipped with a high temperature attachment from data collected at 550 °C on a sample carefully sprinkled. All the *hkl* lines of the corresponding PXRD pattern could be successfully indexed in a conventional unique axis *b* monoclinic cell (a = 5.18890(4), b = 5.85867(5), and c = 12.4260(1) Å, β = 90.2085(4)°) and the study of the systematic absences leads to the $P2_1/c$ space group (no. 14). We notice here that this group is that used by Daniel et al.[20] for the structural description of α-Na_2TeO_4 prepared by hydrothermal conditions from a mixture of NaOH and TeO_2 at 600 °C (10.632, 5.161, and 13.837 Å, β = 103.27°). If those two parameters sets are different, then we can nevertheless remark that the parameter corresponding to the $[TeO_4]_n^{2n-}$ chains is preserved. The refined angle β is very close to 90°, indicating a very small distortion from the orthorhombic structure. Indeed, replacing (a_M, b_M, c_M) by ($-c_O$, a_O, $-b_O$) and neglecting β gives the orthorhombic structure. The Rietveld calculations are then started in the $P2_1/c$ space group with only one Te position transposed simply from *Pbcn* to $P2_1/c$ according to the following:

$$Pbcn,\ 4c\ \text{site} = 0, y, 0.25 \rightarrow P2_1/c,\ 4e\ \text{site} = 0.25, 0, y$$

In this $P2_1/c$ space group, the three atomic coordinates of that 4e site must be refined according to the international tables. After their refinement, Fourier difference calculations revealed clearly six new 4e sites. From the calculated distances between these sites and the Te one, the two first can be attributed to the Na^+ ions, while the last four ones, corresponding to less intense peaks, are related to O^{2-} positions. With this atomic distribution and assuming an isotropic thermal motion for each kind of atom as for the RT study, the refinement (Figure 9) converged quickly to good reliability factors: R_p = 11.5, R_{wp} = 9.49, R_{exp} = 6.26, χ^2=2.30, Bragg R-factor = 4.71. Table 4 gathered the structural results at 550 °C for Na_2TeO_4, while selected interatomic distances are given in Table 2. As in the RT part, the crystal structure at 550 °C (Figure 3) can also be described as built up from infinite $[TeO_4]_n^{2n-}$ chains of $Te^{VI}O_6$ octahedra sharing edges parallel to the a axis (cell parameter close to 5.2 Å). In these chains, the Te−O distances are larger than the room temperature ones, ranging from 1.892(6) to 2.148(7) Å (mean distance: 2.00 and 1.95 Å at RT). Moreover, the $Te^{VI}O_6$ octahedra are quite distorted with edge length varying from 2.52 to 3.03 Å (for comparison: 2.50−2.85 Å at RT), the two shortest (2.50 Å at RT and 2.52 Å at 550 °C) corresponding to the O−O edge shared by two successive TeO_6 octahedra. The $[TeO_4]_n^{2n-}$ chains can be described from Te−O_2−Te rings (Figure 10)

DOI: 10.1021/acs.inorgchem.8b00993
Inorg. Chem. XXXX, XXX, XXX−XXX

Table 3. Normal Mode Frequencies, Calculated and Experimental, and Attributions for Room Temperature Orthorhombic Na_2TeO_4[a]

calcd	ref 13	exp	attribution
800.0 (B_{2g})	796	794	sym. stretch Te−O1
790.3 (A_g)	796	784	
760.7 (B_{1g})	784	759	asym stretch Te−O1
747.4 (B_{3g})	784		
673.0 (B_{1g})	653	666	O2−O2 stretch out of phase along Te−$O2_2$−Te chains
670.9 (B_{3g})	653		
649.5 (B_{2g})	624	642	O2−O2 stretch in phase along Te−$O2_2$−Te chains
647.7 (A_g)	624		
529.6 (B_{1g})	540	522	Te−O2 stretch
523.9 (B_{3g})	539		
522.1 (B_{2g})	529		
519.4 (A_g)	529		
422.4 (B_{3g})	431		O1−Te−O1 wagging
410.1 (B_{2g})			O2−Te−O2 scissor + O1−Te−O1 scissor
400.7 (B_{1g})	411		O1−Te−O1 wagging
399.9 (A_g)	403	390	O2−Te−O2 scissor + O1−Te−O1 scissor
371.0 (B_{2g})	371	356	O1−Te−O1 twisting
345.3 (A_g)	340	334	
	343 (B_{2g})		
324.1 (B_{3g})	324		O1−Te−O1 rocking, O2−Te−O2 rocking, Na (x, z) translation
319.7 (B_{1g})	313	314	
300.3 (A_g)	295	290	Na1 y translation + O2−Te−O2 scissor + O1−Te−O1 twisting
295.2 (B_{2g})	306		O2−Te−O2 scissor + O1−Te−O1 twisting
295.2 (B_{1g})	301		Na1 x translation + O2−Te−O2
283.7 (B_{3g})	284	274	Na1 z translation + O2−Te−O2 rocking + O2−Te−O2 rocking
279 (B_{1g})	256	259	Na1 (x, z) translation + O2−Te−O2 rocking
255.3 (B_{2g})	222	249	Na1 y translation
251.3 (B_{3g})	242	242	Na1 (x, z) translation
236.8 (B_{3g})	221	224	Na1 (x, z) translation + Na2 (x, z) translation
209.7 (A_g)	187	206	Na2 y translation + Te y translation + O2−Te−O2scissor + O1−Te−O1 scissor
206.7 (B_{1g})	236		Na2 (x, z) translation
198.9 (B_{1g})	155		Na1 (x, z) translation + Na2 z translation + O1−Te−O1 wagging
196.0 (B_{3g})	160		Na2(x, z) translation + O1−Te−O1 wagging
189.1 (B_{2g})	165		Na1 y translation + Na2 y translation + O2−Te−O2 y translation
189.0 (A_g)	176	182	Na1 y translation
178.0 (B_{3g})	151		Na1 (x, z) translation + Na2 (x, z) translation
166.6 (B_{2g})	137		Na2 y translation
165.6 (B_{1g})	140		Na1 (x, z) translation + Na2 (x, z) translation
140.2 (A_g)	48	137	Na2 y translation
112.2 (B_{1g})	106	112	Na2 (x, z) translation
91.8 (B_{3g})	103	71	Na2 (x, z) translation
52.7 (B_{1g})	81	46	Na2 (x, z) translation
31.7 (B_{3g})	58	28	Te x translation + O1−Te−O1 rocking + Na1 (x, z translation) + Na2 (x, z) translation

[a]The calculated wavenumbers have been multiplied by a factor of 1.077. Earlier calculations by Cornette[13] are also included.

that are quite similar in the two RT and HT forms: All the characteristic distances and angles are close. Whatever the symmetry (orthorhombic or monoclinic), each ring belongs to a plane and the angle between two successive planes is about 88° (88.53 at RT and 87.34° at 550 °C). The $[TeO_4]_n^{2n-}$ chains are linked together by the sodium cations in an octahedral coordination that is even more distorted than at room temperature: the Na−O distances are ranging from 2.07 to 2.95 Å for Na1 and from 2.26 to 2.93 Å for Na2. The two distances 2.95 and 2.93 Å being very long, one can consider here an (5 + 1) environment instead of an octahedral one. All these results mean that the two forms are very close from a structural point of view.

It has been impossible to obtain the same monoclinic distortion by ab initio calculations. Starting from the experimental values, we obtain a stable structure very close, not to say identical, to the orthorhombic low temperature one (Table 4). Attempts were also made to start with a more deformed structure, by increasing the β angle, but calculations converged always toward a structure very close to orthorhombic, with identical Te−O_2−Te bridges.

Concerning the counting of the Raman-active modes in the monoclinic structure, 42 modes (21 A_g and 21 B_g) are expected as in the orthorhombic one. The A_g and B_{3g} modes of the orthorhombic structure transform into A_g, and B_{1g} and B_{2g} transform into B_g modes. Therefore, no real band splitting is expected at the transition. However, because of the close value

DOI: 10.1021/acs.inorgchem.8b00993
Inorg. Chem. XXXX, XXX, XXX−XXX

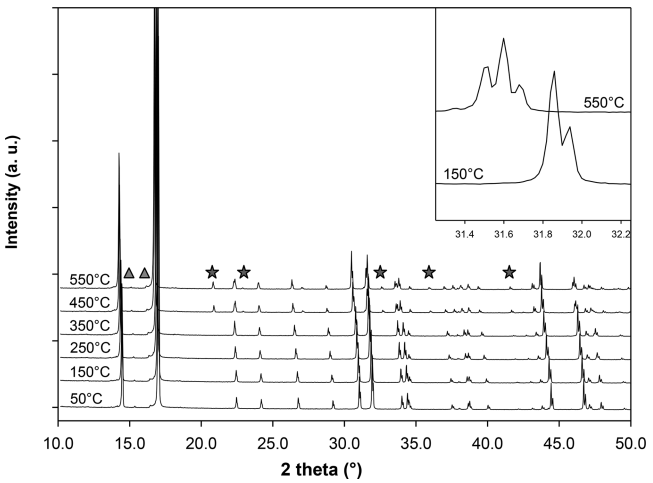

Figure 5. Evolution of β-Na_2TeO_4 PXRD pattern under heating showing the appearance of new *hkl* lines (★) and the splitting of a *hkl* line due to the transition orthorhombic → monoclinic. (▲: Kα3, Kα4, and Kβ contributions). Insert: zoom of the peak splitting resulting of the structural transition. For more clarity, we decided to show only half of the patterns recorded (every 100 °C).

of modes with different symmetries in the orthorhombic structure which transform into modes with the same symmetry, apparent splitting can occur; two bands with the same symmetry and energy interacting to give two new bands separated by a larger gap. This seems to appear in the 400 and 500 cm^{-1} ranges and more clearly near 200 cm^{-1}. A major change in the $[TeO_4]_n^{2n-}$ chains observed at the transition is the appearance of two different Te−O_2−Te bridges, which in turn give rise to two different O−O distances: 2.527 Å for the O3−O3 bond and 2.597 Å for the O4−O4 one. In the orthorhombic structure, we have attributed the band group near 640 cm^{-1} to the stretching of these bonds. We thus expect that two bands will replace the single one at the transition. What we observe is in fact a strong enlargement of the most intense band, from 17−20 cm^{-1} below 400 °C to 30 cm^{-1} above the transition temperature. This could be due to the small difference between both O−O distances. Another feature observed at the transition is the existence of a strong band at very low wavenumbers, near 20 cm^{-1}. A band exists in this region in the orthorhombic structure spectrum, but we have at the moment no explanation for this sudden intensity change at the transition.

Study of the CO_2 Capture. According to our previous works on garnets and Ruddlesden−Popper phases and the observations of Kratochvil et al.,[19] we decided to test the ability of β-Na_2TeO_4 toward the CO_2 capture. This test can be rapidly realized by using this following procedure: A platinum crucible with about 0.3 g of Na_2TeO_4 powder is placed in a reactor (125 cm^3) containing 10 drops of water.[10] A CO_2 pressure of 10 bar is applied, and the reactor is heated at 140 °C for 14 h. After a natural cooling of the furnace, the powder is first dried at 60 °C in an oven before recording a PXRD pattern. This PXRD pattern reveals first the complete disappearance of the mother form β-Na_2TeO_4 (Figure 11a,b). It also shows the presence of $NaHCO_3$ (Powder Diffraction File no. 17−3645, Joint Committee on Powder Diffraction Standards, 2017) and two sets of *hkl* lines, one fine and the other broad. The resulting mixture is then heated under argon flow in a TG analyzer coupled with a mass spectrometer (Figure 12). On heating between RT and 550 °C, the TG curve shows a total mass loss close to 16% with a three steps process: the first step around 120 °C, the second one near 420 °C, and the third one around 475 °C. Each one is clearly associated with simultaneous departure of CO_2 and H_2O. After the TG/MS analysis, the PXRD pattern registered showed only the presence of β-Na_2TeO_4 (Figure 11c) indicating thus that the β-Na_2TeO_4 transformation in humid CO_2 is reversible and that a heating at 550 °C allows to recover entirely the mother phase. At this stage, we tried to find a cell able to index all the *hkl* lines of the PXRD pattern excluding the $NaHCO_3$ ones. This was possible with an orthorhombic cell of parameters $a \approx 4.829$, $b \approx 12.822$ and $c \approx 5.200$ Å (see Figure S2). As expected due to the PXRD pattern characteristics (coexistence of large and thin *hkl* lines), the reliability factors were not satisfying; however, we can nevertheless note that the cell parameters are relatively close to those of the mother Na_2TeO_4: a = 5.75845(2), b = 12.22603(5), and c = 5.18998(2) Å. Moreover, the preserved cell parameter corresponds to the one running along the infinite TeO_6 octahedra chains (≈5.19 Å for the both forms). All these results suggest a strong structural relationship between

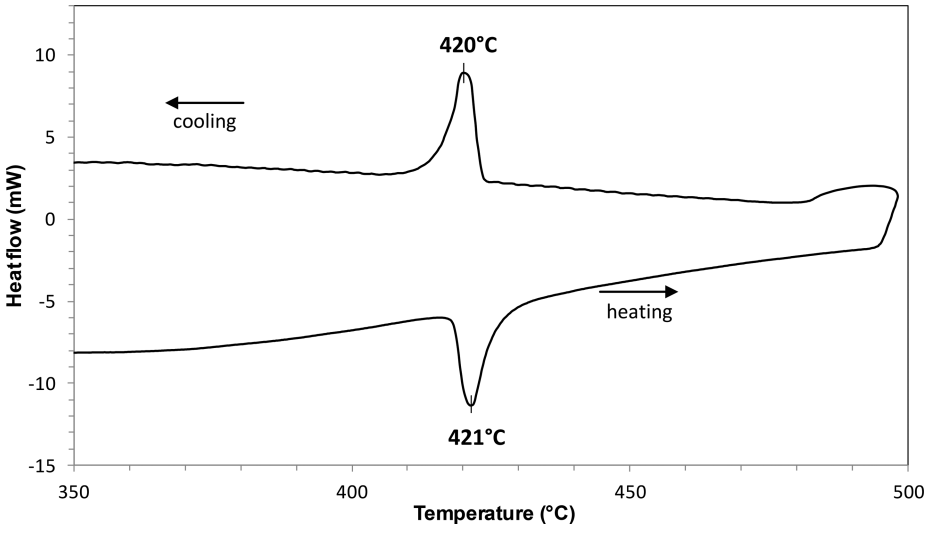

Figure 6. DSC curve showing the endothermic peak associated to the structural transition orthorhombic → monoclinic of β-Na_2TeO_4.

DOI: 10.1021/acs.inorgchem.8b00993
Inorg. Chem. XXXX, XXX, XXX−XXX

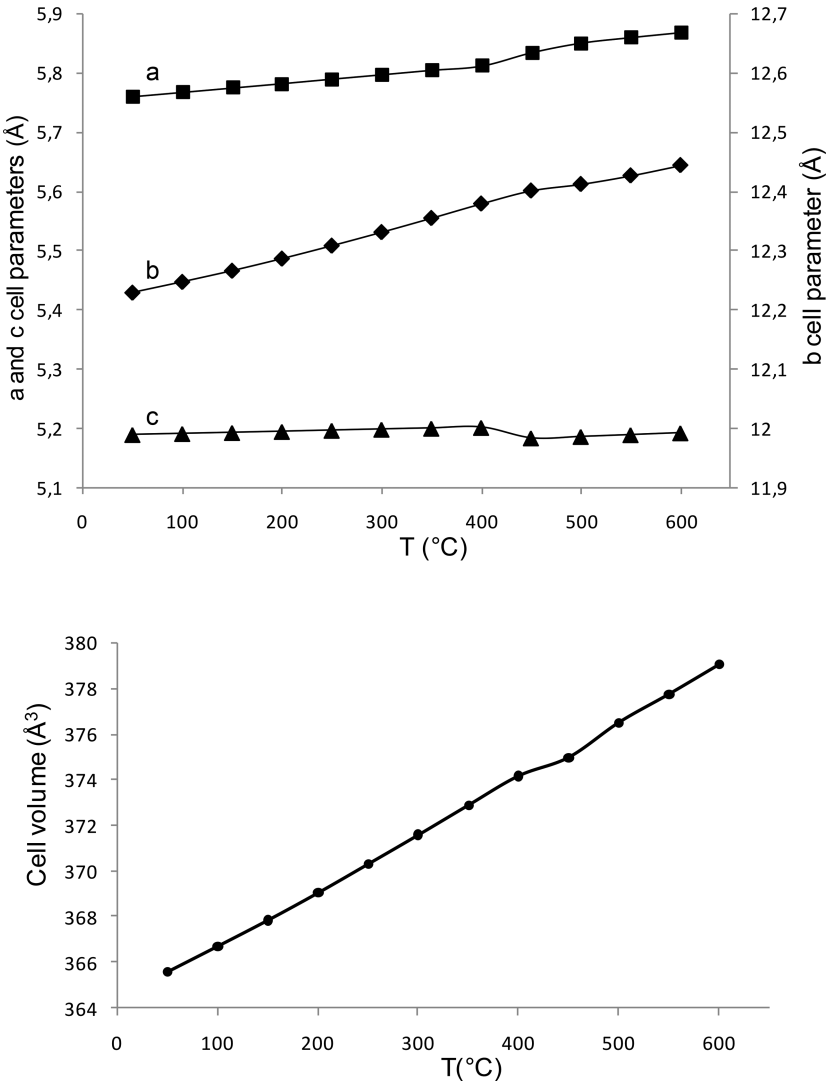

Figure 7. Evolution of the cell parameters (Å) and of the volume (Å^3) of Na_2TeO_4 versus temperature from PXRD data refinements.

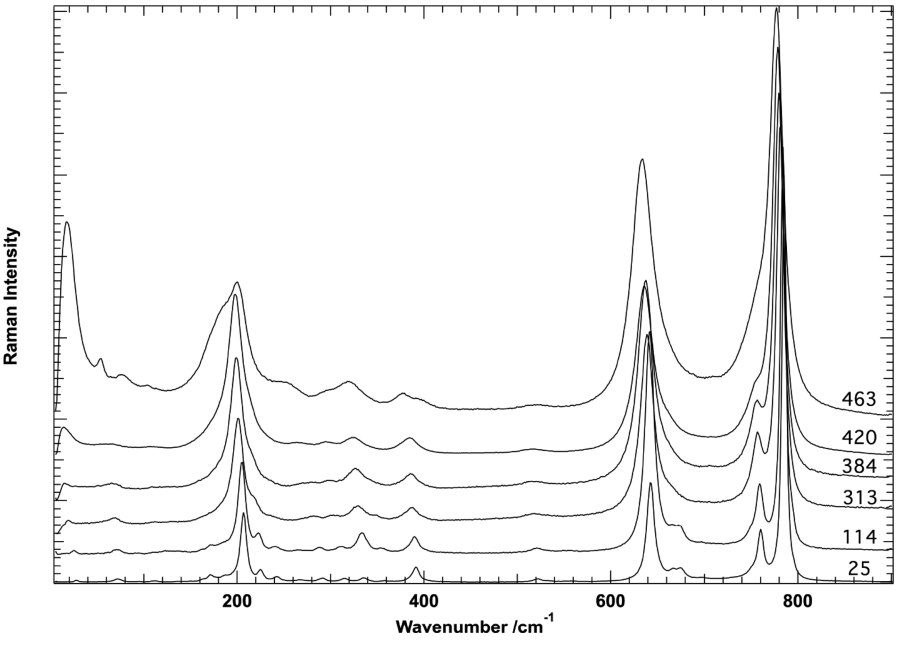

Figure 8. Raman spectra of Na_2TeO_4 at various temperatures (°C) in dry synthetic air.

DOI: 10.1021/acs.inorgchem.8b00993
Inorg. Chem. XXXX, XXX, XXX−XXX

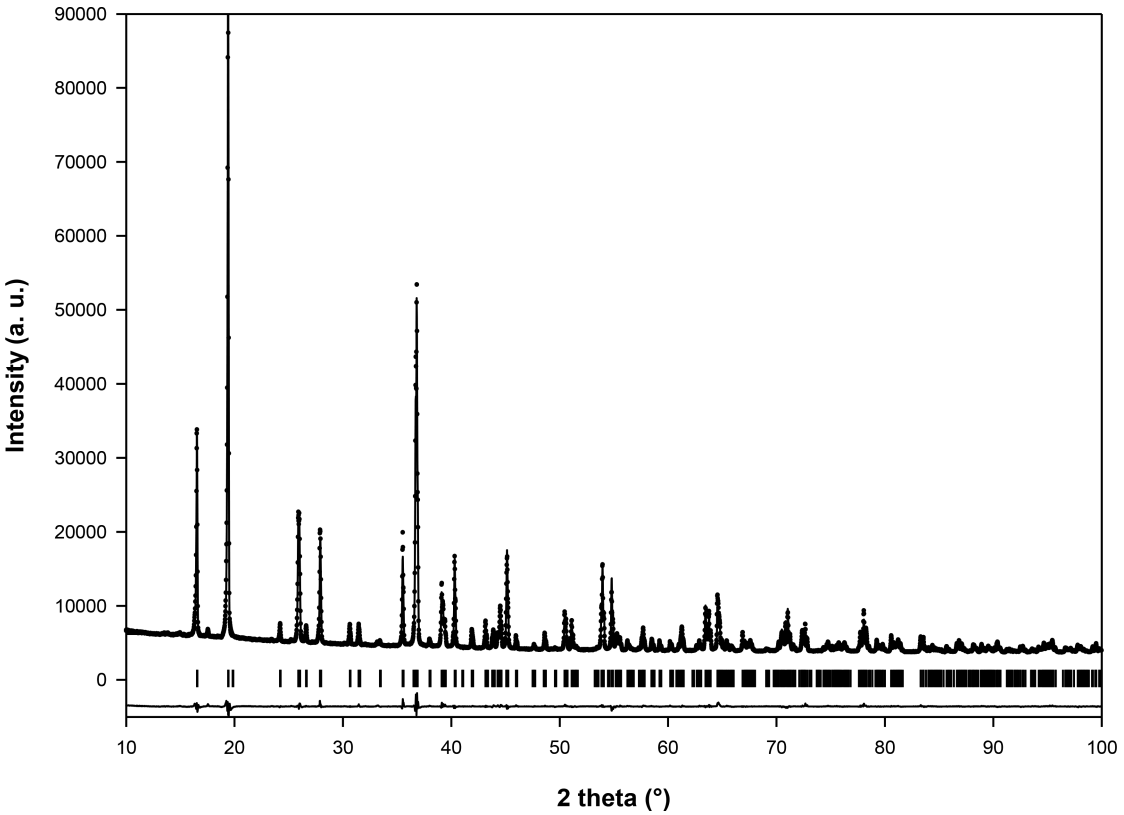

Figure 9. Observed, calculated, and difference PXRD patterns of Na_2TeO_4 at 550 °C in the $P2_1/c$ SG. Vertical bars are related to the Bragg reflection positions.

Table 4. 550 °C Structure Data of Na_2TeO_4 Obtained by Rietveld Refinement[a]

space group $P2_1/c$ (no. 14)
a = 5.18890(4) Å, b = 5.85867(5) Å, c = 12.4260 (1) Å, β = 90.2085 (4)°
[a = 5.2288 Å, b = 5.7566 Å, c = 12.2066 Å, β = 90.0009°]
R_p = 11.5, R_{wp} = 9.49, R_{exp} = 6.26, χ^2 = 2.30, Bragg R-factor = 4.71
η = 0.475(9); half-width parameters: u = 0.044(1), v = −0.0287(7), w = 0.0094(1)

atom	site	x	y	z	B_{iso}
Te	4e	0.2507(2) [0.25000]	0.0329(1) [0.00000]	0.07141(5) [0.07230]	0.67(3)
Na1	4e	0.743(2) [0.75000]	0.0419(8) [0.00000]	0.2356(3) [0.22540]	3.47(8)
Na2	4e	0.209(1) [0.25000]	0.0165(8) [0.00001]	0.3842(3) [0.36099]	3.47(8)
O1	4e	0.373(2) [0.38813]	0.191(2) [0.29815]	0.6487(5) [0.67427]	2.6 (1)
O2	4e	0.869(2) [0.88811]	0.121(1) [0.20182]	0.8046(5) [0.82719]	2.6 (1)
O3	4e	0.435(2) [0.42916]	0.149(2) [0.17992]	0.9319(6) [0.94949]	2.6 (1)
O4	4e	0.949(2) [0.92915]	0.208(2) [0.17992]	0.0291(6) [0.05050]	2.6 (1)

[a]The results of the ab initio calculations are given in square brackets.

the mother phase β-Na_2TeO_4 and the one formed after the ROR experiment. In order to obtain more information on this new phase formed during the CO_2 test, we decide to observe it using a SEM and to perform an EDX analysis. First, we do not observe two types of grains with the retrodiffused electrons detector, thus implying that this sample is homogeneous versus the chemical composition despite the presence of two phases on the corresponding PXRD pattern. We think that each crystallite of Na_2TeO_4 releases Na^+ cations on its entire surface leading to the presence of $NaHCO_3$ on the whole surface of each grain. This seems to be confirmed by the SEM image (see Figure S3) showing a particle consisting of a layer-coated core. Moreover, the EDX analyses of the core and the layer show that the amount of tellurium is very low in the layer compared to that of the core.

All these combined results are in favor of the following mechanism:

$$Na_2TeO_4 + xH_2O + xCO_2 \leftrightarrow Na_{2-x}H_xTeO_4 + xNaHCO_3$$

To check this hypothesis, 0.5 g of Na_2TeO_4 was introduced in 100 mL of water. Under stirring, a nitric acid solution (2 M) was progressively added until the pH remained acidic and constant. After 12 h, the solid product was recovered by filtration, washed with distilled water, and finally dried in an oven at 60 °C. The filtrate obtained after the washing step has then been analyzed with an atomic emission spectrometer. The presence of sodium has been confirmed and corresponded to 71% of the initial sample. A PXRD pattern of the solid has also

DOI: 10.1021/acs.inorgchem.8b00993
Inorg. Chem. XXXX, XXX, XXX−XXX

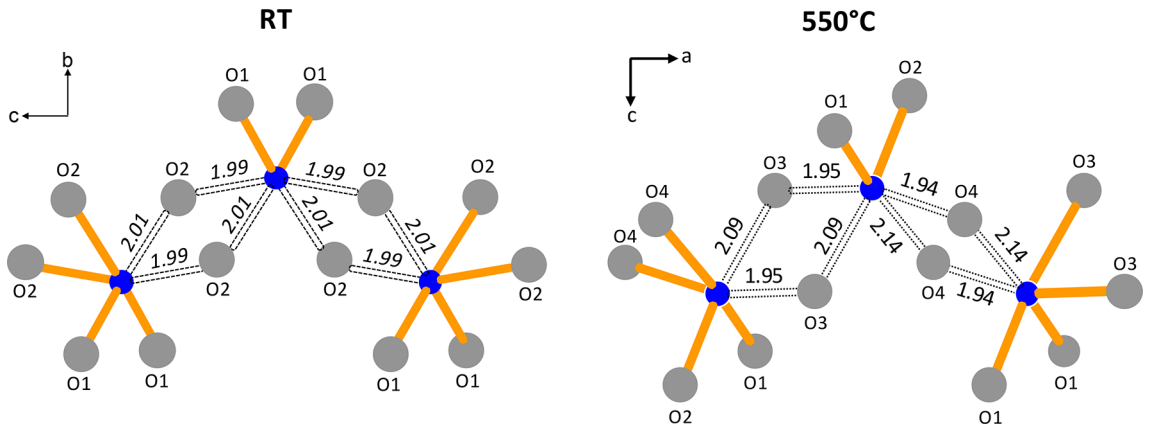

Figure 10. $[TeO_4]_n^{2n-}$ chains showing the Te−O−Te rings with their characteristic distances.

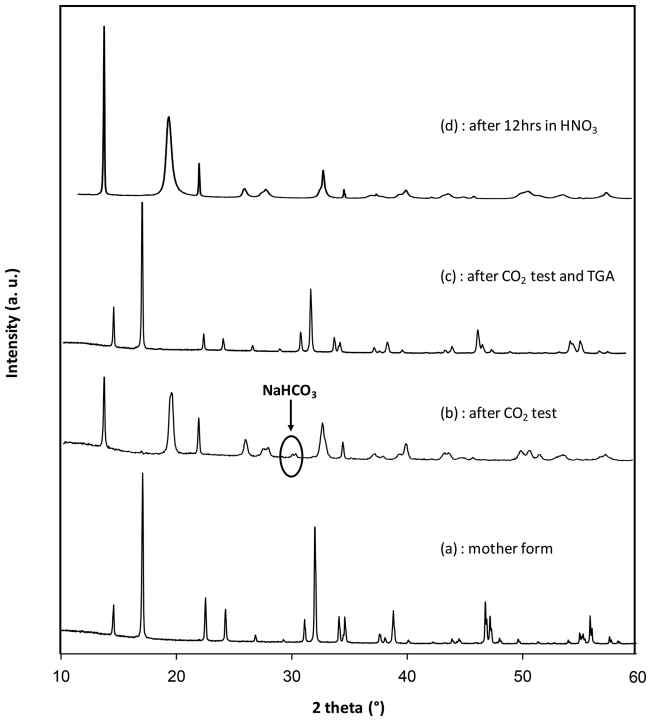

Figure 11. β-Na_2TeO_4 PXRD pattern: mother phase (a), after CO_2 test (b), after CO_2 test and TGA (c), and after 12 h in HNO_3 (d).

been registered: It is similar to that of the compound obtained after the ROR experiment with the coexistence of large and thin *hkl* line (Figure 11d). All these results demonstrate that Na_2TeO_4 allows the reversible CO_2 capture and confirm the proposed mechanism: an ionic Na^+/H^+ exchange leading to the formation of a $Na_{2-x}H_xTeO_4$ phase and $NaHCO_3$.

CONCLUSION

The structure of the β-Na_2TeO_4 orthorhombic form (*Pbcn* space group), prepared via a solid-state reaction from TeO_2 and dried Na_2CO_3, have been studied as a function of temperature between room temperature and 650 °C from PXRD data, DSC analysis, and Raman spectroscopy. Ab initio calculations have also been performed. The room temperature orthorhombic structure has been confirmed and a phase transition occurring near 420 °C toward a monoclinic structure has been highlighted. This transition is fully reversible and the corresponding enthalpy change can be estimated from the DSC peak area as equal to about 7 J g^{-1}. Above 420 °C, Na_2TeO_4 crystallizes in the monoclinic $P2_1/c$ space group, and its structure has been characterized from Rietveld treatment of its powder X-ray diffraction pattern. Whatever the temperature, Na_2TeO_4 structure can be described as built up from infinite chains of TeO_6 octahedra sharing edges and running parallel to the preserved cell axis during heating (close to 5.2 Å, *c* axis in the orthorhombic form, and *a* axis in the monoclinic one). The chains $[TeO_4]_n^{2n-}$ are linked together by the sodium cations in an octahedral coordination whose distortion increases with temperature. The major effect of the transition is to replace identical Te−O_2−Te cycles by two slightly different cycles.

It can be noted here that this transition from an orthorhombic to a monoclinic symmetry is uncommon since in general a heating is associated with a symmetry increase. We can nevertheless find some examples of such unexpected behavior in the literature. For instance, the 3D perovskite $Li_{0.75}Ba_3Nb_{2.25}O_9$ undergoes around 1300 °C a structural transition from a cubic to a hexagonal cell due to an ordering of Li^+ and Nb^{5+} cations, which are distributed on the same crystallographic site at room temperature.[32] More recently, two polymorphs $Li_4B_2O_5$ transforms into each other at about 618 °C: The low-temperature form crystallizes in an orthorhombic cell while that of the high-temperature is monoclinic.[33]

We have also shown that β-Na_2TeO_4 orthorhombic form allows the reversible CO_2 capture through the formation of $NaHCO_3$ by a two-step mechanism:

$$Na_2TeO_4 + xH_2O + xCO_2 \leftrightarrow Na_{2-x}H_xTeO_4 + xNaHCO_3$$

This mechanism shows also that β-Na_2TeO_4 can be used as humidity sensor. Surprisingly, this reaction of β-Na_2TeO_4 orthorhombic form with CO_2 and H_2O is in contradiction with the study of Kratochvil and Jensovsky: For them, Na_2TeO_4 crystals spontaneously rehydrate in wet atmosphere or in water to give $Na_3H_5Te_2O_{10}$.[19]

A structural study of the partially Na^+/H^+ exchanged form $Na_{2-x}H_xTeO_4$ is complex due to the coexistence of large and thin *hkl* lines in the PXRD pattern. However, we were able to propose a set of cell parameters for this compound. As the cell parameter parallel to the chains axis is preserved, it is reasonable to think that the chains $[TeO_4]_n^{2n-}$ are still present in the exchanged form $Na_{2-x}H_xTeO_4$. This work will be the subject of a forthcoming paper.

DOI: 10.1021/acs.inorgchem.8b00993
Inorg. Chem. XXXX, XXX, XXX−XXX

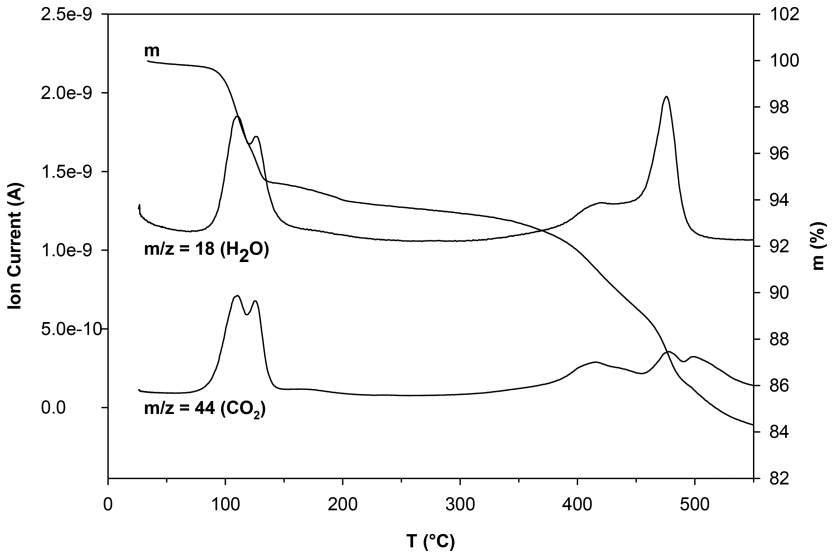

Figure 12. TGA curve and MS results of Na_2TeO_4 after the CO_2 test.

■ ASSOCIATED CONTENT

Ⓢ Supporting Information

The Supporting Information is available free of charge on the ACS Publications website at DOI: 10.1021/acs.inorgchem.8b00993.

Method used to calculate the normal-mode frequencies and atomic displacements, SEM image of the β-Na_2TeO_4 grains, A_g normal modes atomic displacements for β-Na_2TeO_4 at RT, B_{1g} normal modes atomic displacements for β-Na_2TeO_4 at RT, B_{2g} normal modes atomic displacements for β-Na_2TeO_4 at RT, B_{3g} normal modes atomic displacements for β-Na_2TeO_4 at RT, cell parameters (Å) and volume (Å^3) of Na_2TeO_4 obtained by Rietveld refinement every 50 °C between 50 and 600 °C, refinement of the PXRD pattern of the compound after the ROR test and SEM image of a particle after the ROR experiment (PDF)

Accession Codes

CCDC 1812488 contains the supplementary crystallographic data for this paper. These data can be obtained free of charge via www.ccdc.cam.ac.uk/data_request/cif, or by emailing data_request@ccdc.cam.ac.uk, or by contacting The Cambridge Crystallographic Data Centre, 12 Union Road, Cambridge CB2 1EZ, UK; fax: +44 1223 336033.

■ AUTHOR INFORMATION

Corresponding Author

*E-mail: marie-pierre.crosnier-lopez@univ-lemans.fr.

ORCID

Marie-Pierre Crosnier-Lopez: 0000-0002-8676-7063

Notes

The authors declare no competing financial interest.

■ ACKNOWLEDGMENTS

We thank Pr. François Goutenoire (IMMM, Le Mans Université) for helpful discussions about the collection of PXRD data. The diffractometers and the SEM used in this study belong to platforms of the "Institut des Molécules et Matériaux du Mans (IMMM)": "Plateforme de Diffusion et Diffraction des Rayons-X" and "Plateforme de Microscopie Electronique".

■ REFERENCES

(1) Song, C. Global challenges and strategies for control, conversion and utilization of CO_2 for sustainable development involving energy, catalysis, adsorption and chemical processing. *Catal. Today* **2006**, *115*, 2−32.

(2) Zhao, T.; Ochoa-Fernandez, E.; Rønning, M.; Chen, D. Preparation and High-Temperature CO_2 Capture Properties of Nanocrystalline Na_2ZrO_3. *Chem. Mater.* **2007**, *19*, 3294−3301.

(3) Martínez-dlCruz, L.; Pfeiffer, H. Microstructural Thermal Evolution of the Na_2CO_3 Phase Produced during a Na_2ZrO_3−CO_2 Chemisorption Process. *J. Phys. Chem. C* **2012**, *116*, 9675−9680.

(4) Bamiduro, F.; Ji, G.; Brown, A. P.; Dupont, V. A.; Zhao, M.; Milne, S. J. Spray-Dried Sodium Zirconate: A Rapid Absorption Powder for CO_2 Capture with Enhanced Cyclic Stability. *ChemSusChem* **2017**, *10*, 2059−2067.

(5) Martínez-dlCruz, L.; Pfeiffer, H. Cyclic CO_2 chemisorption−desorption behavior of Na_2ZrO_3: Structural, microstructural and kinetic variations produced as a function of temperature. *J. Solid State Chem.* **2013**, *204*, 298−304.

(6) Kato, M.; Nakagawa, K.; Essaki, K.; Maezawa, Y.; Takeda, S.; Kogo, R.; Hagiwara, Y. Novel CO_2 absorbents using lithium containing oxide. *Int. J. Appl. Ceram. Technol.* **2005**, *2*, 467−475.

(7) Togashi, N.; Okumura, T.; Oh-Ishi, K. Synthesis and CO_2 absorption property of Li_4TiO_4 as a Novel CO_2 absorbent. *J. Ceram. Soc. Japan* **2007**, *115*, 324−328.

(8) Kim, H.; Jang, H. D.; Choi, M. Facile synthesis of macroporous Li_4SiO_4 with remarkably enhanced CO_2 adsorption kinetics. *Chem. Eng. J.* **2015**, *280*, 132−137.

(9) Amorim, S. M.; Domenico, M. D.; Dantas, T. L. P.; José, H. J.; Moreira, R. F. P. M. Lithium orthosilicate for CO_2 capture with high regeneration capacity: Kinetic study and modeling of carbonation and decarbonation reactions. *Chem. Eng. J.* **2016**, *283*, 388−396.

(10) Galven, C.; Fourquet, J. L.; Suard, E.; Crosnier-Lopez, M. P.; Le Berre, F. Mechanism of a reversible CO_2 capture monitored by the layered perovskite $Li_2SrTa_2O_7$. *Dalton Trans.* **2010**, *39*, 4191−4197.

(11) Pfeiffer, H.; Vázquez, C.; Lara, V. H.; Bosch, P. Thermal Behavior and CO_2 Absorption of $Li_{2-x}Na_xZrO_3$ Solid Solutions. *Chem. Mater.* **2007**, *19*, 922−926.

(12) Rodriguez, M. T.; Pfeiffer, H. Sodium metasilicate (Na_2SiO_3): A thermo-kinetic analysis of its CO_2 chemical sorption. *Thermochim. Acta* **2008**, *473*, 92−95.

DOI: 10.1021/acs.inorgchem.8b00993
Inorg. Chem. XXXX, XXX, XXX−XXX

(13) Cornette, J. *Cristallochimie et étude vibrationnelle de composés à base de $Te^{VI}O_3$*. Ph.D. Thesis, University of Limoges, Limoges, France, 2010. www.theses.fr/2010LIMO4061.
(14) Galven, C.; Fourquet, J. L.; Crosnier-Lopez, M. P.; Le Berre, F. Instability of the Lithium Garnet $Li_7La_3Sn_2O_{12}$: Li^+/H^+ Exchange and Structural Study. *Chem. Mater.* **2011**, *23*, 1892−1900.
(15) Galven, C.; Dittmer, J.; Suard, E.; Le Berre, F.; Crosnier-Lopez, M. P. Instability of lithium garnets against moisture. Structural characterization and dynamics of $Li_{7-x}H_xLa_3Sn_2O_{12}$ and $Li_{5-x}H_xLa_3Nb_2O_{12}$. *Chem. Mater.* **2012**, *24*, 3335−3345.
(16) Larraz, G.; Orera, A.; Sanjuán, M. L. Cubic phases of garnet-type $Li_7La_3Zr_2O_{12}$: the role of hydration. *J. Mater. Chem. A* **2013**, *1*, 11419−11428.
(17) Wang, W.; Fang, Q.; Hao, G. Reaction mechanisms of $Li_5La_3Ta_2O_{12}$ powder with ambient air: H^+/Li^+ exchange with water. *Adv. Mater. Res.* **2012**, *463*−*464*, 123−127.
(18) Boulant, A.; Bardeau, J. F.; Jouanneaux, A.; Emery, J.; Buzare, J. Y.; Bohnke, O. Reaction mechanisms of $Li_{0.30}La_{0.57}TiO_3$ powder with ambient air: H^+/Li^+ exchange with water and Li_2CO_3 formation. *Dalton Trans.* **2010**, *39*, 3968−3975.
(19) Kratochvil, B.; Jensovsky, L. The crystal Structure of Sodium Metatellurate. *Acta Crystallogr., Sect. B: Struct. Crystallogr. Cryst. Chem.* **1977**, *33*, 2596−2598.
(20) Daniel, F.; Maurin, M.; Moret, J.; Philippot, E. Etude structurale d'un nouveau tellurate alcalin: Na_2TeO_4. Evolution de la coordination du tellure (VI) et du cation quand on passe du cation lithium au sodium. *J. Solid State Chem.* **1977**, *22*, 385−391.
(21) Lapasset, J.; Moret, J. Structure de $SrTeO_4$ sur Monocristal. Organisation de Structures Comportant des Empilements de Chaines $(TeO_4)_n$. Dimorphisme de Na_2TeO_4. *Acta Crystallogr., Sect. C: Cryst. Struct. Commun.* **1985**, *41*, 1558−1562.
(22) Singh, N. K.; Choudhary, R. N. Phase transitions in Na_2TeO_4 ceramics. *Bull. Mater. Sci.* **2000**, *23*, 239−241.
(23) Weil, M.; Stöger, B.; Larvor, C.; Raih, I.; Gierl-Mayer, C. Z. The Hydrous Sodium Oxotellurates $Na[TeO(OH)_5]$, $Na_2[TeO_2(OH)_4]$, $Na_4[Te_2O_6(OH)_4](H_2O)_6$, and a Third Polymorph of Anhydrous $Na_2[TeO_4]$. *Z. Anorg. Allg. Chem.* **2017**, *643*, 1888.
(24) Rietveld, H. M. A Profile Refinement Method for Nuclear and Magnetic Structures. *J. Appl. Crystallogr.* **1969**, *2*, 65−71.
(25) Rodriguez-Carvajal, J. *FULLPROF*, version 5.40; March 2014.
(26) Helwig, A.; Spannhake, J.; Muller, G.; Rosman, N.; Pagnier, T. Temperature characterization of silicon substrates for gas sensors by Raman spectroscopy. *Sens. Actuators, B* **2007**, *126*, 240−244.
(27) Gonze, X.; Beuken, J. M.; Caracas, R.; Detraux, F.; Fuchs, M.; Rignanese, G. M.; Sindic, L.; Verstraete, M.; Zerah, G.; Jollet, F.; Torrent, M.; Roy, A.; Mikami, M.; Ghosez, P.; Raty, J. Y.; Allan, D. C. First-principles computation of material properties: the ABINIT software project. *Comput. Mater. Sci.* **2002**, *25*, 478−492.
(28) Perdew, J. P.; Burke, K.; Ernzerhof, M. Generalized Gradient Approximation Made Simple. *Phys. Rev. Lett.* **1996**, *77*, 3865−3868.
(29) Fuchs, M.; Scheffler, M. Ab initio pseudopotentials for electronic structure calculations for poly-atomic systems using density-functional theory. *Comput. Phys. Commun.* **1999**, *119*, 67−98.
(30) Brese, N. E.; O'Keeffe, M. Bond-Valence Parameters for Solids. *Acta Crystallogr., Sect. B: Struct. Sci.* **1991**, *47*, 192−197.
(31) Shannon, R. D. Revised Effective Ionic Radii and Systematic Studies of Interatomic Distances in Halides and Chalcogenides. *Acta Crystallogr., Sect. A: Cryst. Phys., Diffr., Theor. Gen. Crystallogr.* **1976**, *32*, 751−767.
(32) Collins, B. M.; Jacobson, A.; Fender, B. E. F. Preparation of the Ordered Perovskite-Like Compounds $Ba_4M_3LiO_{12}$ (M = Ta,Nb): A Powder Neutron Diffraction Determination of the Structure of $Ba_4Ta_3LiO_{12}$. *J. Solid State Chem.* **1974**, *10*, 29−35.
(33) He, M.; Okudera, H.; Simon, A.; Köhler, J.; Jin, S.; Chen, X. Structure of $Li_4B_2O_5$: high-temperature monoclinic and low-temperature orthorhombic forms. *J. Solid State Chem.* **2013**, *197*, 466−470.

DOI: 10.1021/acs.inorgchem.8b00993
Inorg. Chem. XXXX, XXX, XXX−XXX